# Study On Temperature-SOC-Current Ternary Coupling Characteristics Of UAV Lithium-Ion Batteries

Lin-yi Zhou and Xin-ji Gan*

*School of Mechanical Engineering,Beihua University, Jilin 132013, China*

*Corresponding author. E-mail: ganxinji@beihua.edu.cn*

*Received: Feb. 9, 2026; Accepted: May. 13, 2026*

In lithium-ion battery systems for UAVs, the ternary coupling relationship between temperature, State of Charge (SOC), and current exerts a decisive impact on battery performance and safety. Through multi-parameter collaborative experiments combined with thermodynamic modeling to analyze the system's energy conversion and heat transfer processes, this study reveals the dynamic evolution laws of the coupling relationship. Experimental results indicate that distinct SOC intervals exhibit significantly differentiated coupling behaviors during constant current discharge. in the high SOC stage ( $80\% - 100\%$ ), the three parameters show an approximately linear relationship. in the medium SOC stage ( $30\% - 80\%$ ), due to the coupling of internal resistance with SOC and heat conduction effects, the temperature presents a non-monotonic "rise-fall-rise again" variation; in the low SOC stage (<30%), a positive feedback loop of "internal resistance-heat generation-temperature rise" is triggered by the strong coupling effect between internal resistance and electrode polarization. Although derived with heat capacity simplification and internal resistance approximation, the explicit solution of the thermal equation derived from thermodynamic modeling can although adopting heat capacity simplification and internal resistance approximation, and only applicable to constant current discharge conditions, can still be applied to battery BMS after engineering adaptation and a hierarchical early warning matrix integrating the current-SOC-temperature relationship is constructed, providing a theoretical and practical application basis for the intelligent thermal management of UAV batteries.

**Keywords:** Lithium-ion batteries for UAVs; Ternary coupling relationship; Thermodynamic modeling; Hierarchical early warning matrix



http://dx.doi.org/10.6180/jase.202610_33.010

## 1. Introduction

As the power core of UAVs, lithium-ion battery performance and safety are dominated by the temperature-SOC-current ternary coupling relationship. Although extensive studies have focused on dual-parameter correlation, the inherent ternary coupling mechanism remains insufficiently understood, restricting the development of reliable battery management. Their dynamic interactions significantly affect battery thermal behavior, aging evolution and operational safety, which necessitates systematic in-depth research.

Thermodynamically, current determines heat generation and serves as a critical basis for SOC estimation. Regulating average current enables collaborative optimization of SOC and SOH [1], and integrating SOC-IC helps improve estimation accuracy under high-rate charging [2]; current correction and fusion estimation algorithms further enhance dynamic SOC tracking capability [3, 4]. Temperature and SOC exhibit strong coupling: temperature variation obviously changes model parameters, and SOC calibration guarantees the reliability of temperature estimation [5]; multi-temperature parameter identification and algorithm optimization support high-precision SOC estimation [6]. Current and temperature jointly dominate battery aging: higher current intensifies heat generation, while high temperature relieves capacity fading under large current but accelerates aging at low current [7, 8]. Experimental results verify that higher current leads to faster temperature rise and higher steady-state temperature [9]. Affected by multi-physics coupling and aging effects, SOC presents obvious nonlinear time-varying characteristics. The high-order nonlinear features of voltage and current during charging and discharging reflect internal state evolution, and polynomial-activated neural networks realize high-precision SOC estimation with limited samples [10]. The ternary coupling also affects battery impedance; screening impedance frequency features strongly correlated with SOH but weakly coupled with SOC, combined with temperature correction, effectively improves battery state estimation accuracy [11]. Under internal short-circuit conditions, temperature, current and SOC change synergistically with internal resistance variation and capacity attenuation, and the electrochemical-thermal coupling model accurately reproduces such parameter evolution [12].

Excessively high temperature degrades charging and discharging performance and reduces SOC estimation accuracy. Novel heat pipe and phase change materials effectively suppress battery temperature rise and meet packaging requirements, providing support for UAV battery active cooling design [13–15]. Meanwhile, UAV wireless charging technologies have been widely studied; various positioning and system schemes improve charging power and operational stability [16–19], and existing reviews have summarized relevant theories, application scenarios and technical specifications [20]. Nevertheless, most current studies concentrate on charging topology and power transmission efficiency, while neglecting the ternary coupling effect under dynamic charge-discharge conditions, which impair charging performance and thermal characteristics and limits BMS development. Accordingly, this paper explores the dynamic coupling mechanism of temperature, current and SOC in the medium current range through experiments and thermodynamic modeling, aiming to provide theoretical and technical support for thermal management, state estimation and safety control of UAV lithium-ion batteries.

## 2. Theory and formula

### 2.1. Construction of Thermodynamic Model

Based on the first law of thermodynamics (energy conservation), the heat balance equation states that the rate of heat change inside the battery equals the generated heat minus the dissipated heat, as shown in Eq. (1).

$$\frac{dU}{dt} = Q_{\text{gen}} - Q_{\text{loss}} \tag{1}$$

where $U$ is the internal thermal energy of the battery, and $dU = C(T)dT$ (definition of heat capacity). $C(T)$ is the equivalent average total heat capacity of the internal battery system, which is a nonlinear heat capacity that usually changes with temperature. However, it approximately varies linearly near room temperature, so a linear model $C(T) = C_0[1+ \propto (T - T_0)]$ is adopted for simplification. Here $C_0 = 107\ \mathrm{J/K}$ is the heat capacity at the reference temperature $T_0 = 25°\mathrm{C}$, and $\propto = 0.002\ \mathrm{K}^{-1}$ is the temperature coefficient (obtained by fitting experimental data). Substituting these values gives Eq. (2).

$$Q_{gen} = I^2 R(S,T) + Q_{rev} \tag{2}$$

Where $I^2R(S,T)$ is the Joule heat with $R$ denoting the internal resistance coupled to both SOC and temperature. Derived from the equivalent circuit model and empirical fitting, the complete internal resistance model, combining SOC-dependent and temperature-dependent components, is expressed as shown in Eq. (3).

$$R(S,T) = \left[R_{const} + R_{low}e^{k_1 S} + R_{high}e^{k_2(S-100)}\right] \cdot \left[1 + \beta\left(T - T_{ref}\right)\right] \tag{3}$$

Where $R_{const} = 0.0165\Omega$ (initial battery resistance), $R_{low} = 0.016\Omega, k_1 = -0.03, R_{high} = 0.013\Omega, k_2 = 0.065$ (obtained by regression of experimental data using the least square method to fit charge-discharge curves). And the temperature coefficient $\beta = 0.0012\ \mathrm{K}^{-1}$ are calibrated via least squares regression of experimental charge-discharge curves, with $T_{ref} = 25°\mathrm{C}$ as the reference temperature. The three-term SOC-dependent part captures resistance variations across low, medium, and high SOC ranges, while the linear temperature factor simplifies the Arrhenius relation for practical engineering implementation.In Eq. (2), $Q_{rev}$ represents the thermal effect caused by the reversibility of electrochemical reactions during battery charging and discharging. Its formula is shown in Eq. (4).

$$Q_{\text{rev}} = -0.02 \cdot I \cdot T \cdot \frac{ds}{dt} \tag{4}$$

where $I$ is the discharge current (A); $T$ is the instantaneous battery temperature ( °C ); $\frac{ds}{dt}$ is the rate of SOC change ( %/ min ); - 0.02 is the proportional constant obtained by fitting experimental data. $Q_{loss}$ in Eq. (1) is convective heat loss, expressed in Eq. (5).

$$Q_{loss} = hA\,(T - T_0) \tag{5}$$

Substituting $Q_{gen}$ and $Q_{loss}$ into Eq. (1) and simplifying gives the temperature-SOC-current coupling formula shown in Eq. (6).

$$C(T)\frac{dT}{dt} = I^2 R(S,T) + Q_{rev} - hA\,(T - T_0) \tag{6}$$

where $C(T)\frac{dT}{dt}$ is the battery heat accumulation rate (J); $I^2R(S,T)$ is the Joule heat (J); $Q_{rev}$ is the reversible reaction heat (J); $h$ is the convective heat transfer coefficient $\left(\mathrm{W}/\left(\mathrm{m}^2 \cdot \mathrm{K}\right)\right)$; A is the battery heat dissipation area $\left(\mathrm{mm}^2\right)$; $T_0$ is the initial battery temperature $({}^\circ\mathrm{C})$. For engineering simplification, $hA$ is used directly as an overall parameter and dynamically calibrated through experimental temperature rise data. The range of $hA$ is 0.104 0.120 W/°C (calibrated experimentally).

### 2.2. Model Simplification and Engineering Application

The real-time SOC is denoted as $S_t$, which is defined as the ratio of remaining charge. Based on charge conservation (coulomb counting method), it is calculated as shown in Eq. (7).

$$S_t = S_0 - \frac{I}{Q_n} t \times 100\% \tag{7}$$

To simplify the solution of the thermal equation, the arithmetic mean method is used to calculate the average internal resistance $R_{avg}(t)$ at time $t$, as shown in Eq. (8).

$$R_{avg}(t) = \frac{1}{t}\int_0^t R(S(\tau))d\tau \approx \frac{R\left(S_0\right) + R\left(S_t\right)}{2} \tag{8}$$

This transformation is based on the trapezoidal rule of numerical integration. Assuming that internal resistance changes linearly with SOC (the error is negligible when is small), the time-varying internal resistance is simplified to an explicit time function. Since $S_t$ is a linear function, $S_t = S_0 - kt$ where $k = \frac{I}{270} \times 100\%(\%/\min)$. Then $R\left(S_t\right) = R\left(S_0 - kt\right)$ (using the expression of the internal resistance model at $T_{ref}$ ). Since the heat balance equation couples temperature $T$ and SOC through $R(S,T)$, direct solution is difficult. Therefore, drawing on the research conclusions of References [5] and [21], the following reasonable simplifications are made: assume $C(T) \approx$ constant (ignore nonlinearity; replace $R(S,T)$ with $R_{\mathrm{avg}}(t)$ and ignore the temperature dependence of $R$; assume $Q$ rev is constant. The simplified equation is shown in Eq. (9).

$$C(T)\frac{dT}{dt} = I^2 R_{avg}(t) - hA\,(T - T_0) + Q_{rev} \tag{9}$$

where $R_{avg}(t) = \frac{R(S_0)+R(S_0-kt)}{2}$, $S_t = S_0 - \frac{It}{270} \times 100\%$ and $hA$ is the overall heat dissipation parameter (ranging from 0.104 to 0.120 W/°C, calibrated experimentally).Dividing both sides of Eq. (14) by $C(T)$ and rearranging gives a standard linear ordinary differential equation (first-order linear nonhomogeneous ODE), as shown in Eq. (10).

$$\frac{dT}{dt} + aT = b(t) \tag{10}$$

$b(t) = \frac{I^2 R_{avg}(t) - hAT_0 + Q_{rev}}{C}$ Where $a = \frac{hA}{C}$ ( constant, unit: $\mathrm{s}^{-1}$), which clarifies its time dependence and provides a specific expression for ODE solution.). The simplifications (e.g., neglecting internal resistance's temperature dependence, Refs. [5, 21]) are reasonable engineering choices for low-computation, high-real-time UAV BMS, retaining the core ternary coupling law; focusing on revealing the staged coupling mechanism rather than a fully unsimplified model, minor errors are acceptable. Calibrated for the typical UAV operating range $(10 - 30^\circ\mathrm{C}$, covering most civil scenarios), the thermodynamic model adapts to 0°C/40°C extreme conditions via dynamic calibration of $hA$ and the heat capacity temperature coefficient, with extended analyses confirming its applicability despite changes in internal resistance, heat dissipation, and polarization, meeting engineering accuracy requirements. The standard form of the firstorder linear nonhomogeneous ODE is shown in Eq. (11).

$$\frac{dT}{dt} + P(t)T = Q(t) \tag{11}$$

where $P(t) = a$ (constant) and $Q(t) = b(t)$. Multiplying both sides of the ODE by the integrating factor, transforming the equation, integrating both sides, and rearranging terms yields the explicit solution of temperature as a function of time (the time-domain response solution), as shown in Eq. (12).

$$T(t) = e^{-at}\left(\int_0^t b(\tau)e^{a\tau}d\tau + T_0\right) \tag{12}$$

substituted $b(t) = \frac{\frac{R(S_0)+R(S_0-kt)}{2} - hAT_0 + Q_{rev}}{C}$ into Eq. (12) gives the complete solution form in Eq. (13).

$$T(t) = e^{-at}\left(\int_0^t \left[\frac{\frac{R(S_0)+R(S_0-kt)}{2} - hAT_0 + Q_{rev}}{C}\right] e^{a\tau}d\tau + T_0\right) \tag{13}$$

The temperature time-domain response solution quantifies the multi-parameter coupling (current-SOC-internal resistance-temperature) of UAV lithium-ion batteries under constant current discharge, verifying the ternary coupling's phased characteristics and revealing temperature rise mechanisms under varying currents, while resolving the high computational complexity of traditional nonlinear models for UAV BMS. Converting core formulas into basic recursive subfunctions and the early warning matrix into a callable logic table, it requires no additional hardware, adapts to low end microcontrollers, and enables 100 ms real time temperature prediction to support thermal runaway warning, meeting flight safety's demands for both timeliness and accuracy.

## 3. Experimental setup

A 3 S lithium-ion UAV battery module ( 4.5Ah, 11.1 V ) was tested using a setup comprising a high-precision constant-current discharge tester (error $\leq \pm 0.1\%$ ), a 1 Hz data acquisition system, and a temperature sensor ( $0.1^{\circ}\mathrm{C}$ resolution) to measure current, surface temperature, voltage, and discharge capacity. The module was wrapped in aluminum film insulation to eliminate ambient interference. Ten constant-current discharge conditions ( $4.5-9$ A ) were implemented. Prior to testing, equipment was calibrated, sensors were fixed on inter-cell heating zones, and the battery was fully charged at 0.5 C and rested for 2 h to eliminate polarization. Each test involved 30 min of constant-current discharge with real-time temperature monitoring, and the battery was returned to room temperature between tests. All data were recorded synchronously, and the setup is illustrated in Fig. 1.

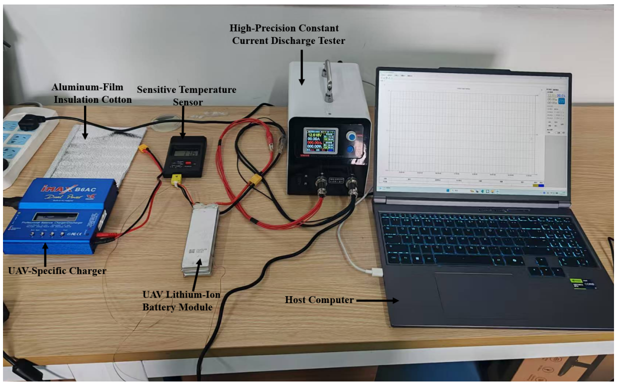


**Fig. 1.** The physical objects of various equipment and devices used in the experiment.

## 4. Result discussions

### 4.1. Model Validation Method and Accuracy Evaluation

Model prediction accuracy is quantified via relative error (Eq. (14)), with temperature prediction errors at 10,20 , and 30 min under 4.5-9A constant current discharge are verified, as shown in Fig. 2. The average error is 1.53% and the maximum error is 2.4%, showing an upward trend with increasing current. the 10 min error peaks at approximately 2.4% under high currents ( $8-9$ A ) due to initial transient heat conduction and polarization effects: early discharge heat concentration leads to unsteady heat conduction deviating from the model's steady-state assumption, while transient polarization resistance changes under high current are not fully captured by the average internal resistance model, causing heat generation prediction deviation. Despite this, errors remain within engineering acceptable ranges, confirming that the temperature-SOC-current coupling model accurately characterizes battery temperature and SOC dynamic responses under different currents, with good accuracy and engineering applicability, providing reliable support for lithium-ion battery thermal management system design.

$$\delta(t, I)=\left|\frac{T_{\text{pred}}(t, I)-T_{\text{mean}}(t, I)}{T_{\text{mean}}(t, I)}\right| \times 100\% \tag{14}$$

where: $T_{\text{pred}}(t, I)$ is the model-predicted temperature ($^{\circ}\mathrm{C}$), and $T_{\text{mean}}(t, I)$ is the experimentally measured temperature ( $^{\circ}\mathrm{C}$ ).

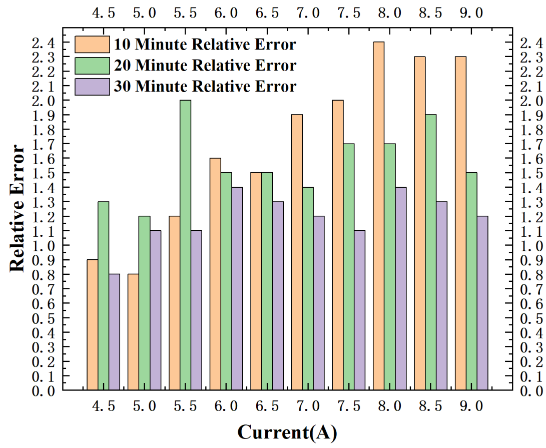


**Fig. 2.** Relative Error Diagram between Predicted and Measured Temperatures.

### 4.2. Construction of Fitting Surface and Early Warning Matrix

To further quantify the global temperature-current-SOC coupling relationship and promote the engineering application of the theoretical model, a quadratic polynomial fitting surface is established via the nonlinear least square method based on 300 groups of sample data acquired from ten constant current discharge tests. In this fitting model, temperature is defined as the dependent variable, while current and SOC are set as independent variables, and the specific fitting function is presented in Eq. (15).

$$f(x, y ; \theta)=a+b x+c y+d x^{2}+e x y+f y^{2} \tag{15}$$

The fitting coefficients were obtained through sample iterative optimization: ( $a = 19.0261$, $b = 2.9835, c = -0.0253, d = -0.0611, e = -0.0225, f = 0.0003$).

With $R^2 = 0.964$ and RMSE $= 0.838°C$, the model achieves high-precision fitting of the temperature-current-SOC coupling relationship, meeting engineering prediction requirements. Centrally distributed near-zero residuals indicate negligible systematic bias, validating its use in real-time BMS temperature estimation. The fitted surface in Fig. 3 characterizes coupling behavior and identifies high-risk zones under high current, low SOC, and elevated temperature. As the dominant factor, current aggravates temperature rise and SOC decay with each 1A increment (especially above 7A), while the negative temperature-SOC correlation increases thermal management difficulty. Discharge currents of $4.5 - 5.5$ A suit long-endurance, thermally stable operation, whereas 8-9 A discharge causes sharp temperature rise and rapid SOC depletion, threatening battery lifespan and safety. Calibrated at room temperature across 4-10 A and $0\% - 100\%$ SOC, the model adapts to varying ambient temperatures via dynamic adjustment of the heat dissipation parameter $hA$ and temperature-dependent heat capacity coefficient.

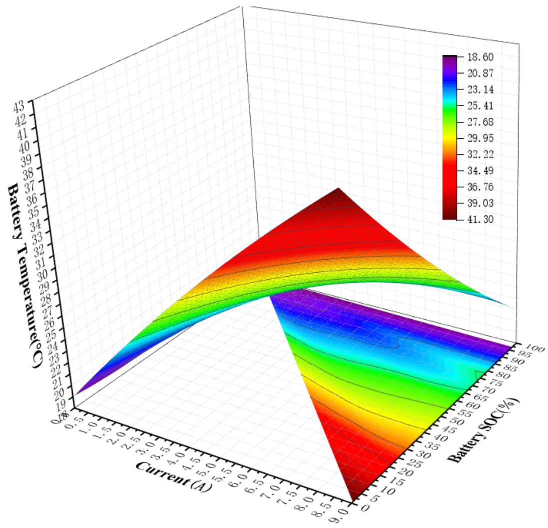


**Fig. 3.** Battery Temperature-SOC-Current Fitting Surface Diagram.

Taking temperature as the core variable, the hierarchical early warning matrix is established based on the fitting formula and surface analysis, as listed in Table 1. Benchmarked at the UAV normal operating temperature range of 10-30°C, the fitting surface and constructed early warning matrix well meet the safety control requirements of conventional operating conditions. The matrix converts temperature–current–SOC coupling characteristics into real-time executable rules for BMS, which supports rapid thermal risk identification and graded regulation to balance UAV flight endurance and battery service life. Changes in ambient temperature affect heat exchange efficiency and electrode polarization, leading to the drift of coupling risk thresholds. low temperatures advance the trigger of thermal risks, whereas high temperatures reduce the threshold of thermal runaway early warning.

### 4.3. Battery Temperature–Current–SOC Coupling Characteristics and 3D Scatter Diagram

As shown in Figs. 4 and 5, battery temperature rises synchronously with SOC decline during constant current discharge, with discharge current as the dominant influencing factor. At 4.5 A , temperature increases by 0.12°C per 1%SOC, while at 9 A , this rate reaches 0.23°C per 1% SOC ( 1.9 times faster), with a 10.1°C rise within 10 minutes once SOC drops below 50%. Driven by internal resistance-SOC coupling and heat generation-dissipation balance, temperature follows a "rapid rise-transient fall-accelerated rise" trend: high initial resistance causes early-stage heating, enhanced heat dissipation leads to a mid-SOC transient drop, and intensified polarization accelerates heating at low SOC.

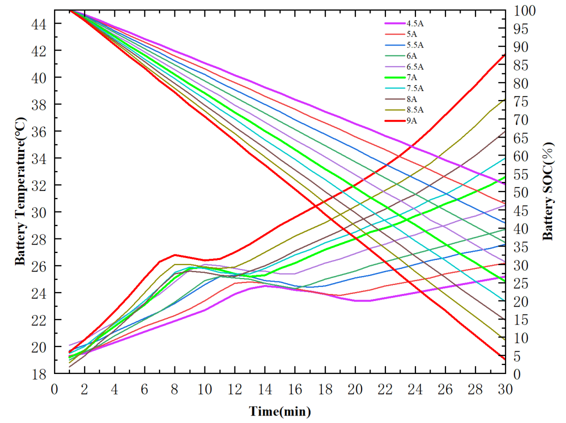


**Fig. 4.** Battery Temperature–Current–SOC Coupling Relationship Diagram.

From the 3D scatter characteristics (Fig. 5), the temperature-SOC-current coupling arises from electro-thermal-chemical interactions: current accelerates SOC decay, while Joule heat (proportional to $I^2$ ) drives temperature rise. Above 35°C, increased internal resistance triggers a positive feedback loop of intensified heat generation. The three parameters show a nonlinear correlation: each 1A increase in current raises the temperature-SOC change rate by an average of 11.8%, and coupling strength increases 3.5 -fold from 4.5 A to 9 A. Temperature is positively correlated with discharge current and negatively correlated with SOC,

**Table 1.** Early Warning Matrix.

| current range (A) | SOC > 80% | SOC30%-80% | SOC < 30% |
|---|---|---|---|
| 4.5-5.5 | Low risk ( $Z < 28°C$ ):<br>Regular discharge<br>Medium risk | Low risk ( $Z < 32°C$ ):<br>Normal heat dissipation<br>Medium risk | Medium risk ( $Z < 35°C$ ):<br>Monitor temperature<br>High risk |
| 6-7.5 | ( $Z < 32°C$ ):<br>Strengthen monitoring | ( $Z < 36°C$ ):<br>Active heat dissipation | ( $Z < 39°C$ ):<br>Reduce current to below 5A |
| 8-9 | ( $Z < 36°C$ ):<br>Limit discharge $\leq$ 15 min | ( $Z < 39°C$ ):<br>Forced liquid cooling | risk ($Z \geq 39°C$) :<br>Trigger overdischarge protection |

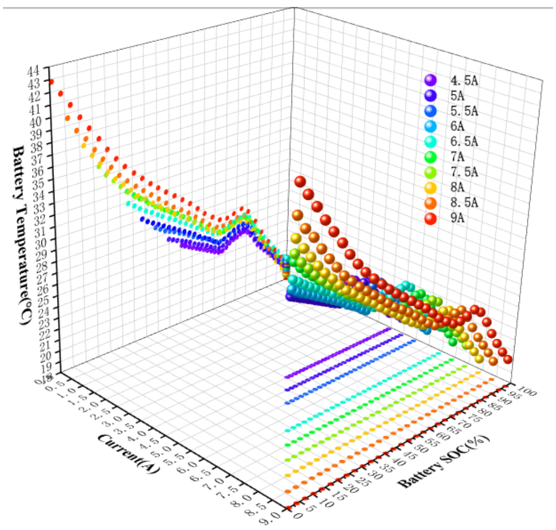


**Fig. 5.** Battery Temperature-Current-SOC 3D Scatter Characteristic Diagram.

providing intuitive support for multi-parameter thermal characteristic analysis.

## 5. Conclusions

This study reveals the staged temperature-SOC-current ternary coupling mechanism of UAV lithium-ion batteries under constant current discharge based on experimental tests and thermodynamic modeling. At high SOC of $80\% - 100\%$, electrothermal characteristics maintain slow temperature rise, linear SOC attenuation and stable parametric coupling; at medium SOC of $30\% - 80\%$, heat generation-dissipation dynamics and electrochemical feedback lead to a non monotonic temperature variation trend; at low SOC below 30%, intensified electrode polarization increases internal resistance and triggers a vicious cycle of thermal accumulation. Discharge current governs coupling strength: $4.5 - 5.5$ A ensures mild temperature growth and stable operation, while current above 7A exacerbates nonlinear coupling and requires matched thermal management and dynamic regulation, with the coupling essence lying in multi physical field interactions among electrochemical reaction, heat generation and capacity decay. The established simplified thermodynamic model and explicit solution balance prediction accuracy and computational efficiency, satisfying the low power and real time requirements of embedded BMS. The hierarchical early warning matrix and regulation strategy enable effective thermal risk identification and control, improving battery thermal safety and service life. This work offers theoretical support and technical reference for the design and safe operation of UAV battery thermal management systems, and future research will incorporate ambient temperature to optimize model performance and expand engineering applicability.

## Acknowledgements

The authors would like to thank all contributors who supported this work.

## References

**[1]** G. Chen, X. Xia, X. Zhao, X. Zeng, T. Ouyang, and H. Feng, (2025) *"A balanced SOH-SOC control strategy for multiple battery energy storage units based on battery lifetime change laws"* **Electrical Engineering** ***107***(6): 7725–7736. DOI: 10.1007/s00202-024-02944-1.

**[2]** R.-P. Zhang, X.-G. Shi, D.-C. Wei, Y.-q. Wang, W. Yin, and Y. Cheng, (2025) *"Multistage Variable Current Pulse Charging Strategy Based on Polarization Characteristics of Lithium-Ion Battery"* **IEEE Transactions on Energy Conversion** ***40***(1): 422–436. DOI: 10.1109/TEC.2024.3446168.

**[3]** W. Q. T. Poh, Y. Xu, W. Liu, and R. T. P. Tan, (2025) *"Momentary informatics based data-driven estimation of lithium-ion battery health under dynamic discharging currents"* **Journal of Power Sources** ***629***: 236041. DOI: 10.1016/j.jpowsour.2024.236041.

**[4]** Y. Zhang, X. Lai, X. Zhang, Y. Fan, E. Cheng, Y. Zheng, X. Tang, B. Tang, and Z. Zhu, (2025) *"Fusion of stress and electrical signals for high-accuracy joint estimation of SOC and SOH in lithium-ion batteries"* **Energy** ***331***: 137063. DOI: 10.1016/j.energy.2025.137063.

**[5]** X. Zhang, Y. Wang, and Z. Chen, (2023) *"SoC-modified core temperature estimation of lithium-ion battery based on control-oriented electro-thermal model"* **IEEE transactions on power electronics** ***38***(9): 11642–11651. DOI: 10.1109/TPEL.2023.3288539.

**[6]** A. Tabine, A. Elachhab, S. Bouzaid, C. Ennawaoui, A. Hajjaji, et al., (2024) *"A novel fitting polynomial approach for an accurate SOC estimation in Li-ion batteries considering temperature hysteresis"* **E-Prime-Advances in Electrical Engineering, Electronics and Energy** ***10***: 100822. DOI: 10.1016/j.prime.2024.100822.

**[7]** L. Jiang, Y. Huang, Y. Li, J. Yu, X. Qiao, C. Huang, and Y. Cao, (2020) *"Optimization of variable-current charging strategy based on SOC segmentation for Li-ion battery"* **IEEE Transactions on Intelligent Transportation Systems** **22**(1): 622–629. DOI: 10.1109/TITS.2020.3006092.

**[8]** J. Qu, Z. Jiang, and J. Zhang, (2022) *"Investigation on lithium-ion battery degradation induced by combined effect of current rate and operating temperature during fast charging"* **Journal of Energy Storage** **52**: 104811. DOI: 10.1016/j.est.2022.104811.

**[9]** I. Permana, A. P. Agharid, F. Wang, and S. H. Lin, (2023) *"Performance investigation of thermal management system on battery energy storage cabinet"* **Thermal Science** **27**(6 Part A): 4389–4400. DOI: 10.2298/TSCI221227154P.

**[10]** M. Yang, H. Shi, Y. Zhu, Y. Zou, L. Xiong, and Q. Huang, (2026) *"A novel polynomial-activated neural network with locally weighted scatterplot smoothing for small-sample state-of-charge estimation in lithium-ion batteries"* **Journal of Energy Storage** ***149***: 120325. DOI: 10.1016/j.est.2025.120325.

**[11]** J. Lee, M. Lee, S. Cho, Y. Kim, J. Oh, and J. Kim, (2026) *"Enhanced battery state of health estimation with long short-term memory employing analytic hierarchy process and the extraction of multi-criteria optimized impedance factors"* **Journal of Energy Storage** ***152***: 120588. DOI: 10.1016/j.est.2026.120588.

**[12]** L. Wang, J. Wu, C. Ma, X. Sun, L. Wang, and C. Liao, (2026) *"Coupling Model and Early-Stage Internal Short Circuits Fault Diagnosis for Gel Electrolyte Lithium-Ion Batteries"* **Batteries** ***12***(2): 45. DOI: 10.3390/batteries12020045.

**[13]** A. Esmaeilzadeh, M. Silakhori, N. N. Nik Ghazali, H. S. C. Metselaar, A. Bin Mamat, M. S. Naghavi Sanjani, and S. Iranmanesh, (2020) *"Thermal performance and numerical simulation of the 1-pyrene carboxylic-acid functionalized graphene nanofluids in a sintered wick heat pipe"* **Energies** ***13***(24): 6542. DOI: 10.3390/en13246542.

**[14]** S. Rangasamy, R. R. V. Raghavan, R. M. Elavarasan, and P. Kasinathan, (2023) *"Energy analysis of flattened heat pipe with nanofluids for sustainable electronic cooling applications"* **Sustainability** ***15***(6): 4716. DOI: 10.3390/su15064716.

**[15]** W. Li, T. Yang, L. Chen, J. Shi, T. Zhang, C. Zeng, R. Liu, and S. Tang, (2025) *"Thermal management study of cylindrical battery using novel thermally conductive anisotropic flexible phase change material"* **Case Studies in Thermal Engineering** ***73***: 106508. DOI: 10.1016/j.csite.2025.106508.

**[16]** P. K. Chittoor and B. Chokkalingam, (2023) *"Wireless electrification system for photovoltaic powered autonomous drone charging"* **IEEE Transactions on Transportation Electrification** ***10***(2): 3002–3011. DOI: 10.1109/TTE.2023.3305022.

**[17]** P. K. Chittoor and C. Bharatiraja, (2023) *"Building integrated photovoltaic powered wireless drone charging system"* **Solar Energy** ***252***: 163–175. DOI: 10.1016/j.solener.2023.01.056.

**[18]** A. Nair, C. Bharatiraja, S. Devakirubakaran, et al. "Pv-powered wireless drone charging station assisted with tracked-vision". In: *2023 Second International Conference on Electrical, Electronics, Information and Communication Technologies (ICEEICT)*. IEEE. 2023, 1–5. DOI: 10.1109/ICEEICT56924.2023.10157708.

**[19]** P. K. Chittoor and C. Bharatiraja, (2022) *"Wireless-sensor communication based wireless-charging coil positioning system for UAVs with maximum power point tracking"* **IEEE Sensors Journal** **22**(8): 8175–8182. DOI: 10.1109/JSEN.2022.3156089.

**[20]** P. K. Chittoor, B. Chokkalingam, and L. Mihet-Popa, (2021) *"A review on UAV wireless charging: Fundamentals, applications, charging techniques and standards"* **IEEE access** ***9***: 69235–69266. DOI: 10.1109/ACCESS.2021.3077041.

**[21]** B. Sun, D. Song, H. Ruan, W. Zhang, and K. Zheng, (2023) *"Parameter identification method of thermal model of lithium-ion battery based on self-generated heat and external heat transfer"* **Transactions of China Electrotechnical Society** ***39***: 278–288. DOI: 10.19595/j.cnki.1000-6753.tces.222104.